Supplementary Information for

Flexible Bi_2Te_3/PEDOT nanowire sandwich-like film towards high-performance wearable cross-plane thermoelectric generator and temperature sensor array

Minzhi Du[a,b], Jianyong Ouyang[*b,c] and Kun Zhang[*a]

[a] Key Laboratory of Textile Science & Technology (Ministry of Education), College of Textiles, Donghua University, Shanghai 201620, PR China

[b] Department of Materials Science and Engineering, National University of Singapore, 9 Engineering Drive 1, Singapore 117576

[c] National University of Singapore (Suzhou) Research Institute, No. 377 Linquan Street, Suzhou Industrial Park, Suzhou, Jiangsu 215123, PR China

[*]Corresponding author. Email: mseoj@nus.edu.sg (J. Ouyang); kun.zhang@dhu.edu.cn (K. Zhang)

Contents

Supplementary schemes, figures, explanatory notes, and tables including:

Bi_2Te_3@PEDOT NW film.

Fig. S10. (a) Optical photograph, (b) FESEM image, and (c) pore size statistics of the porous PDMS supporting substrate.

Fig. S11. (a) Open-circuit voltage (b) total power and the maximum output power density as a function of temperature difference of the cross-plane TEG.

Fig. S12. (a) Schematic diagram of a cross-plane temperature sensor. (b) Temperature sensing performance reflected by the real-time thermovoltage at different temperature differences within 1 K. Stability at different large temperature differences with respect to (c) heating time and (d) heating-cooling cycles.

Fig. S13. Demonstration of the temperature-sensing performance by covering different sensing units with a human finger.

Fig. S14. Conformance and flexibility characterization of the cross-plane sensor array. (a) Illustration of the test diagram. (b) Optical photographs of the cross-plane sensor array attached on PLA tubes with different radii.

Explanatory note 1. Theoretical calculation process of open-circuit voltage of the cross-plane TEG.

Explanatory note 2. Calculation process of the power generation and the maximum power output of the cross-plane TEG.

Explanatory note 3. Detailed estimation of the detected temperature by each sensing unit of the cross-plane sensor array.

Table S1. Elemental compositions of p-type and n-type Bi_2Te_3 powders.

Table S2. FESEM-EDS elemental analysis for p-type 15vol.%-Bi_2Te_3@PEDOT NW film.

Table S3. Component ratios of p-type Bi_2Te_3@PEDOT NW sandwich-like films.

Table S4. Comparison of TE properties in this work with the data of organic/inorganic composite TE materials reported in the literature at room temperature.

Table S5. Theoretical and measured open-circuit voltage of the cross-plane TEG.

Table S6. Total power and the maximum output power of the cross-plane TEG.

Table S7. The detailed data and calculating process of **Fig. 5d**.

Supplementary references (1-26)

Supplementary schemes, figures, explanatory notes, and tables

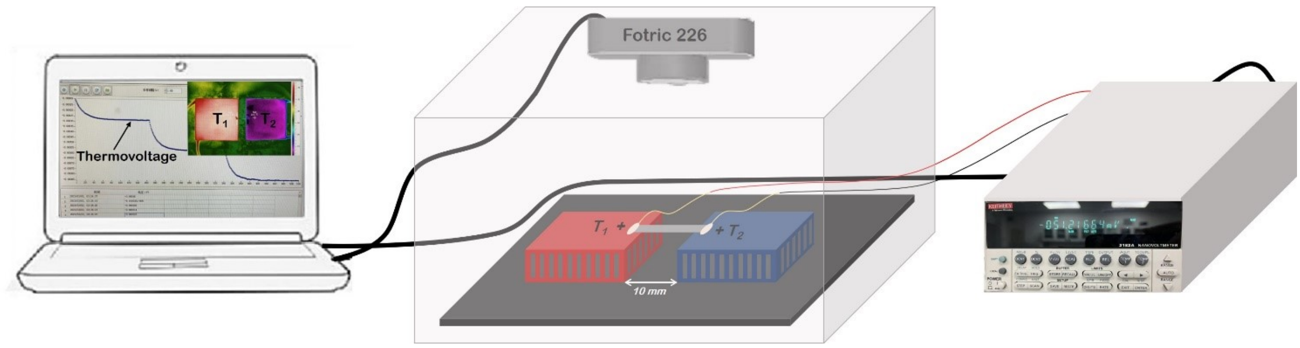

Scheme S1. Illustration of the Seebeck coefficient measurement.

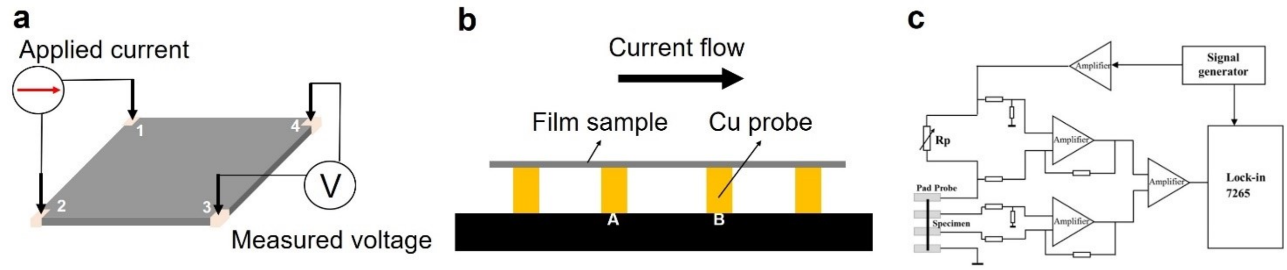

Scheme S2. (a) Illustration of the electrical conductivity measurement using a standard van der Pauw method. (b-c) Illustration of the thermal conductivity measurement and the measurement principles of the self-heating 3ω method.

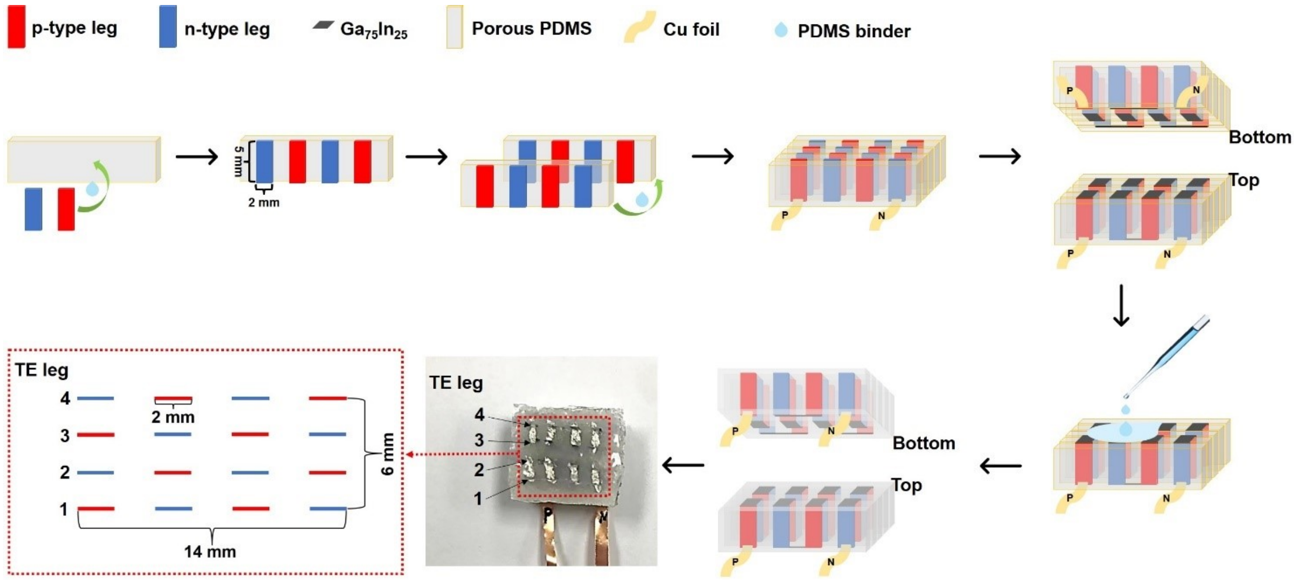

Scheme S3. Illustration of the fabrication process of the cross-plane TEG.

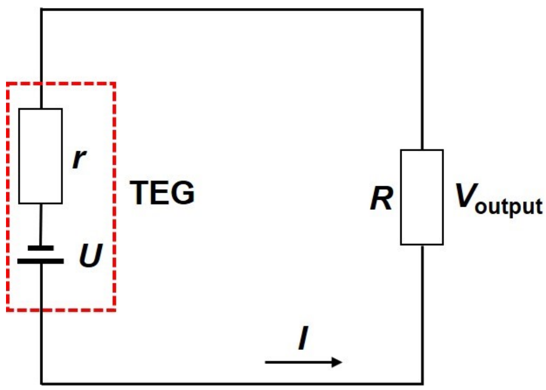

Scheme S4. Equivalent circuit diagram of the cross-plane TEG with an external resistance.

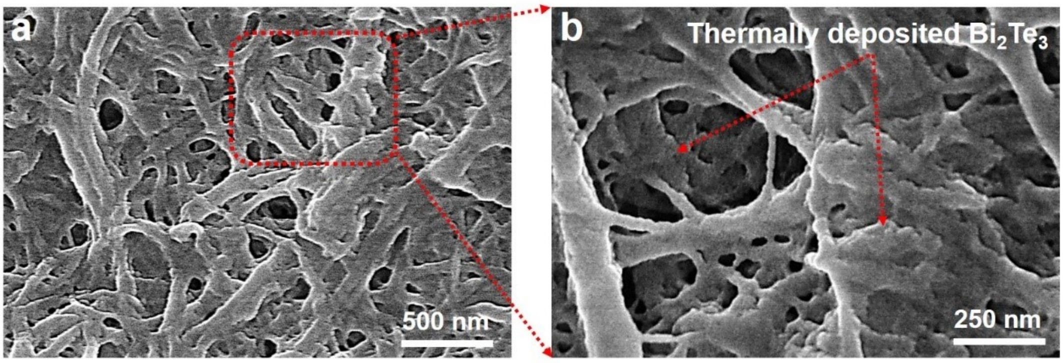

Fig. S1. FESEM images of (a) thermally deposited 10 nm-Bi_2Te_3@PEDOT NW film and (b) the magnified image.

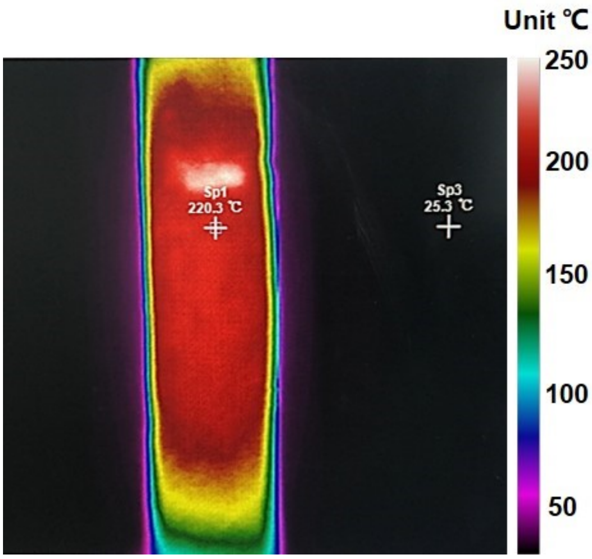

Fig. S2. Temperature of the carbon paper surface when applied with a current of 3.5 A during the thermal shock treatment.

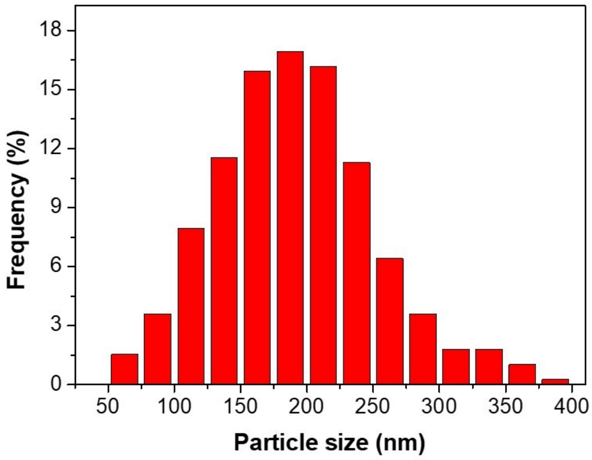

Fig. S3. Particle size distribution of thermal-shocked Bi_2Te_3 nanocrystals.

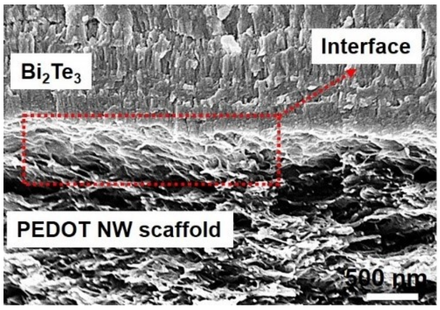

Fig. S4. Cross-sectional FESEM image of p-type 15 vol.%-Bi_2Te_3@PEDOT NW film showing the interface of Bi_2Te_3 and PEDOT NW scaffold.

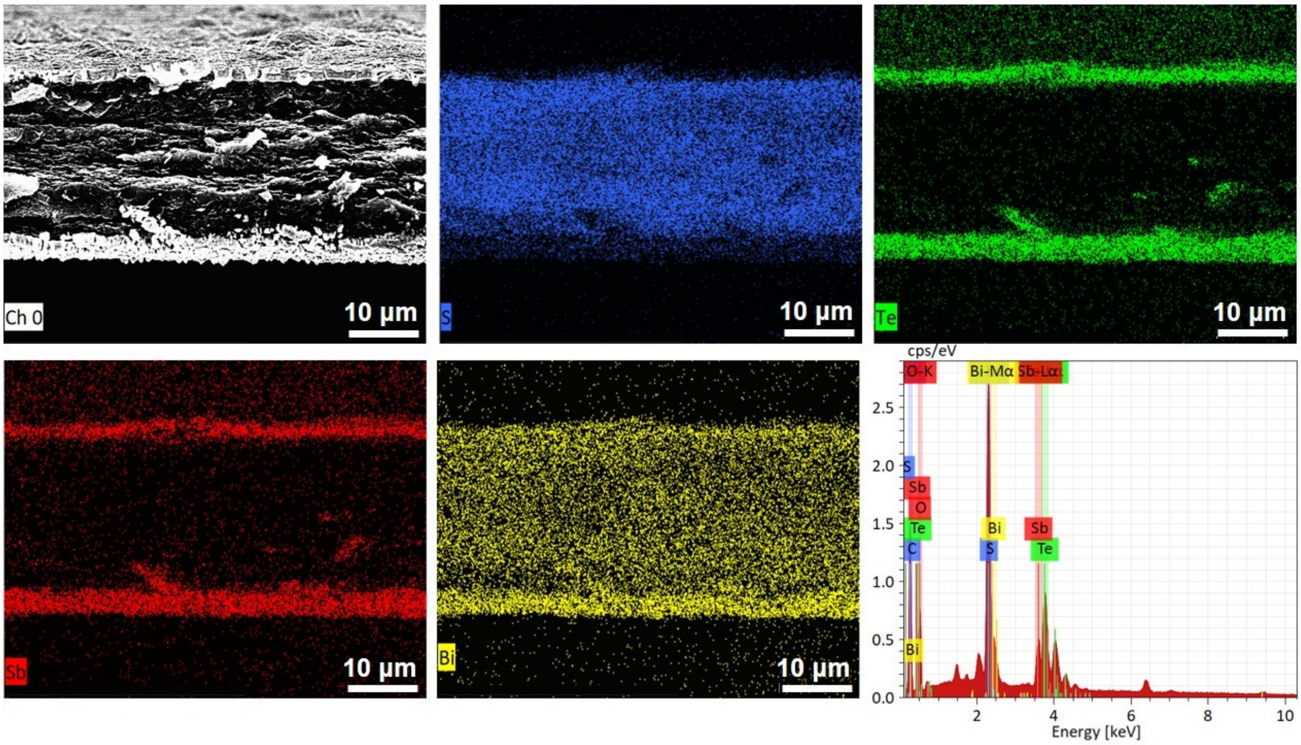

Fig. S5. Individual FESEM-EDS elemental mapping patterns for characteristic elementals in p-type 15 vol.%-Bi_2Te_3@PEDOT NW film.

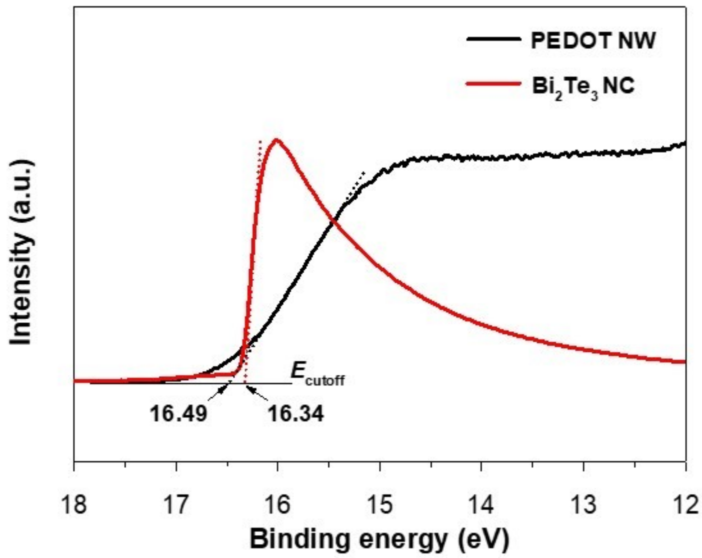

Fig. S6. UPS spectra of PEDOT NW and Bi_2Te_3 nanocrystal in the secondary electron cutoff region.

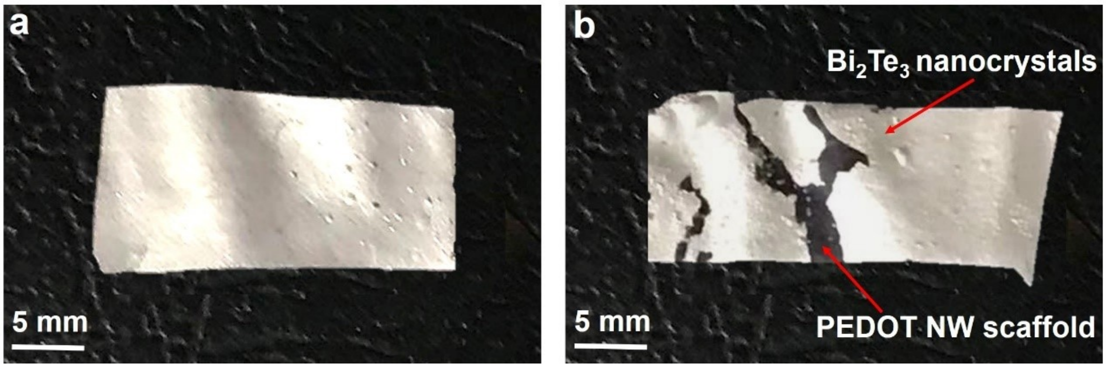

Fig. S7. Optical photographs of thermal-shocked p-type (a) 15 vol.%-Bi_2Te_3@PEDOT NW film and (b) 21.5 vol.%-Bi_2Te_3@PEDOT NW film.

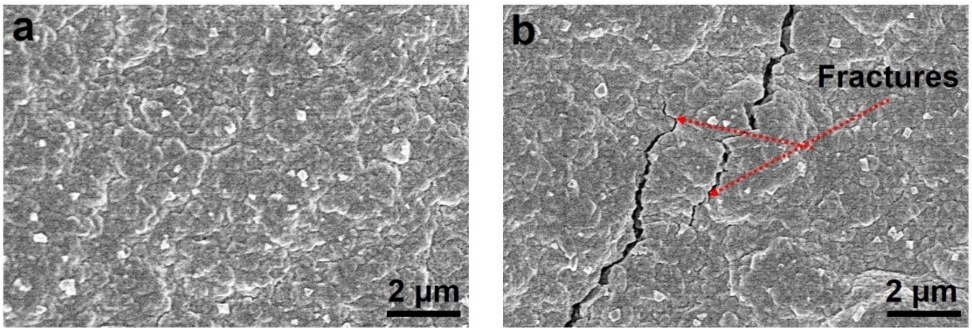

Fig. S8. FESEM images of the surface view of p-type 15 vol.%-Bi_2Te_3@PEDOT NW film (a) before and (b) after bending for 100 cycles at a radius of 7.5 mm.

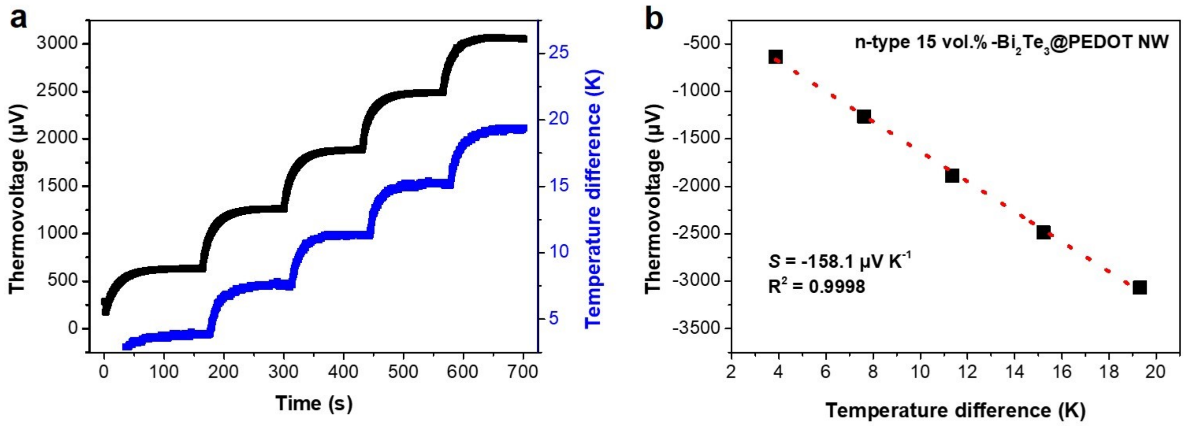

Fig. S9. (a) Thermovoltage profiles and (b) Seebeck coefficient determination of the n-type 15 vol.%-Bi_2Te_3@PEDOT NW film.

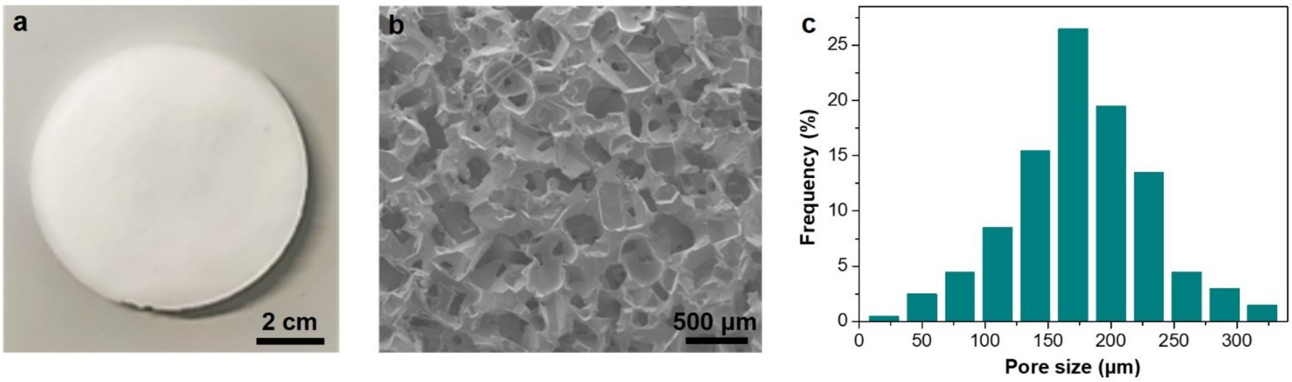

Fig. S10. (a) Optical photograph, (b) FESEM image, and (c) pore size statistics of the porous PDMS supporting substrate.

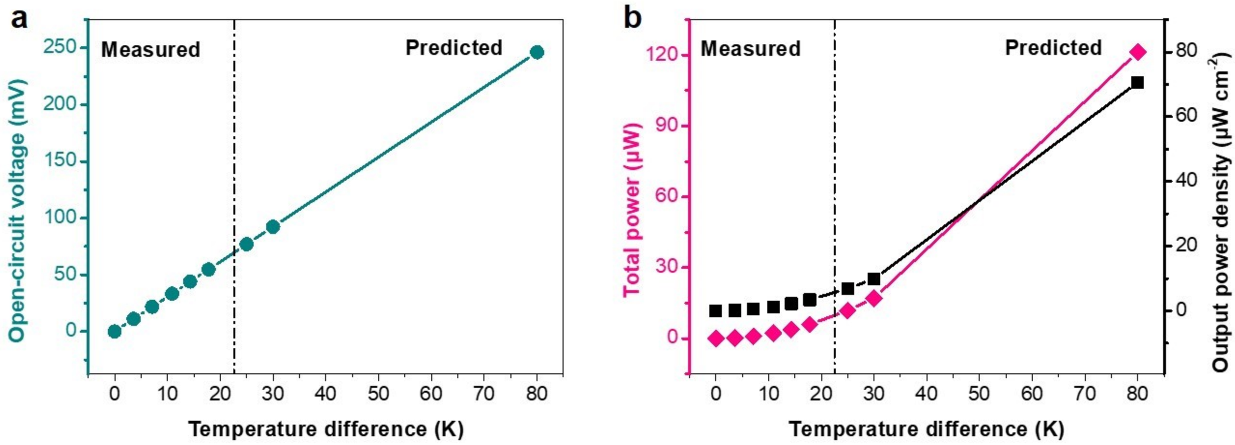

Fig. S11. (a) Open-circuit voltage (b) total power and the maximum output power density as a function of temperature difference of the cross-plane TEG.

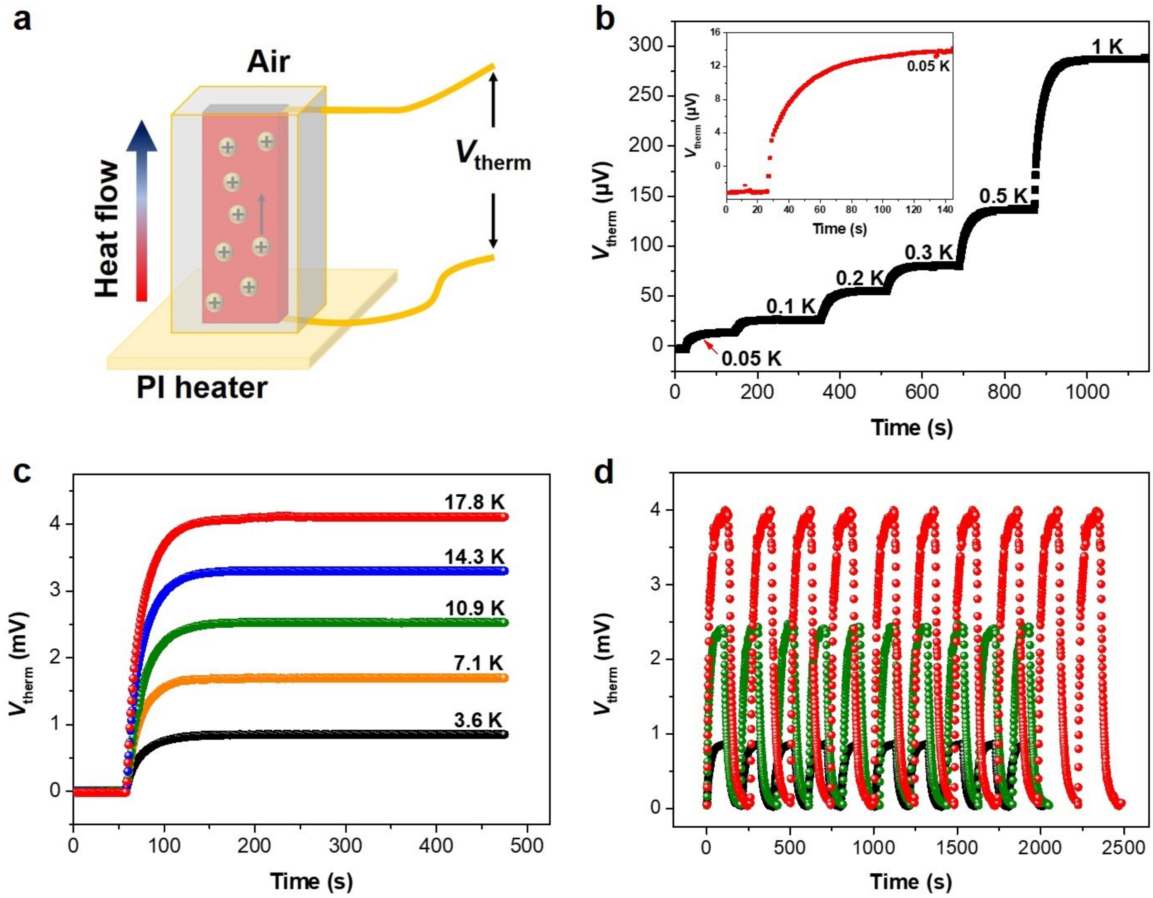

Fig. S12. (a) Schematic diagram of a cross-plane temperature sensor. (b) Temperature sensing performance reflected by the real-time thermovoltage at different temperature differences within 1 K. The insert shows the magnified response signal to a temperature difference of 0.05 K. Stability at different large temperature differences with respect to (c) heating time and (d) heating-cooling cycles.

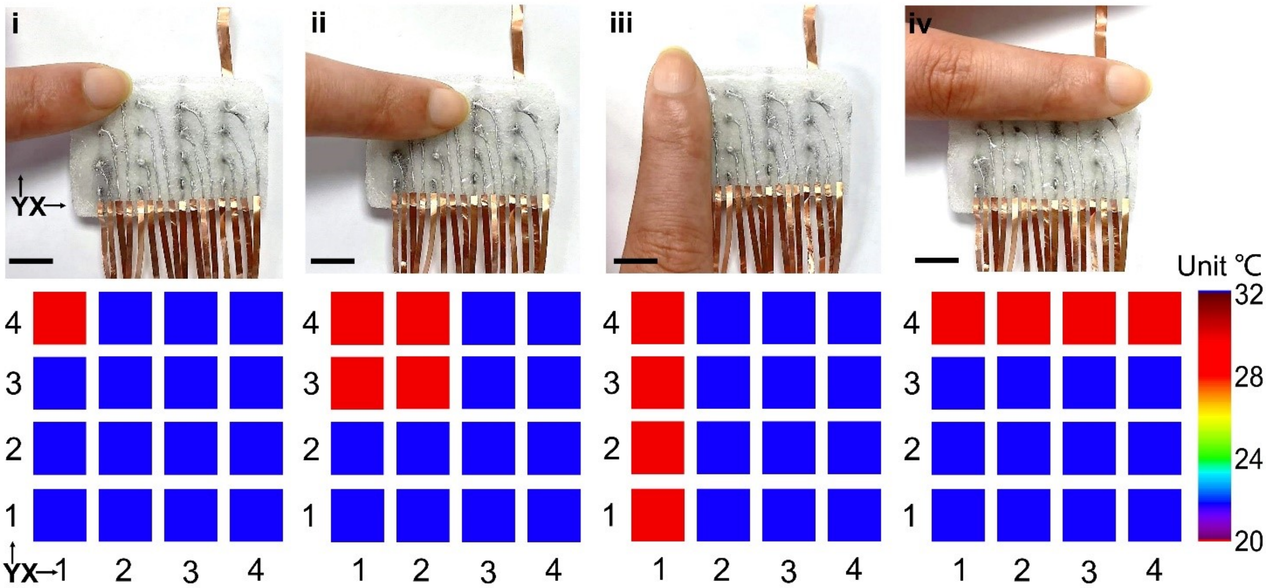

Fig. S13. Demonstration of the temperature-sensing performance by covering different sensing units with a human finger. The ambient temperature is 21.8℃ and the surface body temperature is 29.8℃. All scale bars are 10 mm.

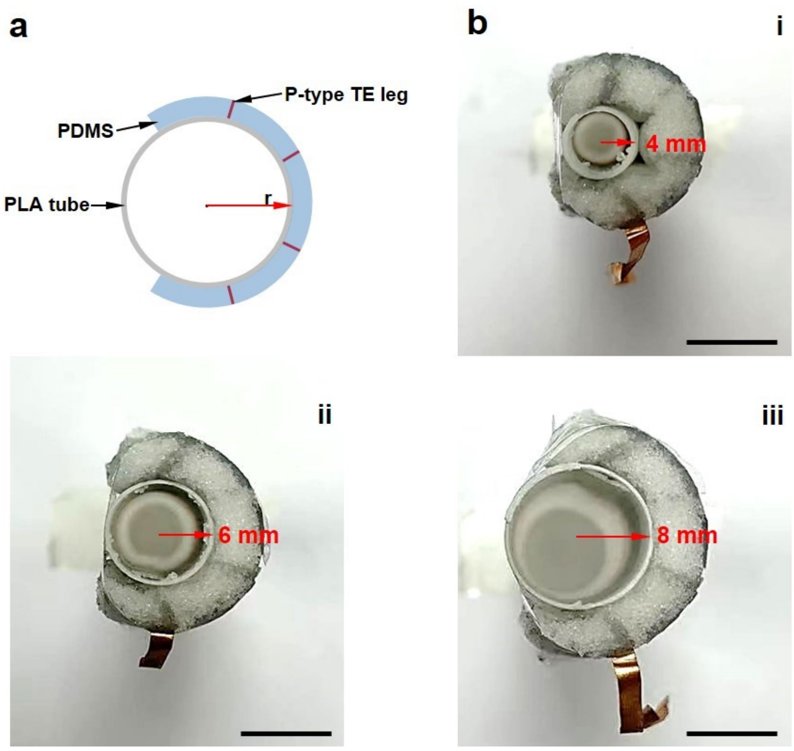

Fig. S14. Conformance and flexibility characterization of the cross-plane sensor array. (a) Illustration of the test diagram. (b) Optical photographs of the cross-plane sensor array attached on PLA tubes with different radii. All scale bars are 10 mm.

Explanatory note 1

Theoretical calculation process of the open-circuit voltage of the cross-plane TEG

The theoretical open-circuit voltage ($V_{oc\text{-}th}$) of the as-prepared cross-plane TEG can be estimated by $V_{oc\text{-}th} = (|S_p| + |S_n|) \times \Delta T \times N$. Where S_p is the Seebeck coefficient of p-type TE leg (0.2664 mV K^{-1}), S_n is the Seebeck coefficient of n-type TE leg (-0.1581 mV K^{-1}), and N is the number of p-n pairs (8). $V_{oc\text{-}th} = 8 \times (0.2664 + 0.1581) \times \Delta T = 3.396\Delta T$. Hence, when ΔT is 3.6 K, 7.1 K, 10.9 K, 14.3 K, and 17.8 K, $V_{oc\text{-}th}$ can be 12.226 mV, 24.112 mV, 37.016 mV, 48.563 mV, and 60.449 mV. Providing that the ΔT of 25 K and 30 K are applied, corresponding $V_{oc\text{-}th}$ of 84.900 mV and 101.880 mV can be calculated.

Due to the slight heat conduction and variation of TE legs, the measured open-circuit voltage ($V_{oc\text{-}m}$) is 11.186 mV, 21.772 mV, 33.366 mV, 44.038 mV, and 54.706 mV. Therefore $V_{oc\text{-}th}$-$V_{oc\text{-}m}$ relation can be linearly fitted as $V_{oc\text{-}m} = 0.9065V_{oc\text{-}th} + 0.039$ ($R^2 = 0.99995$). Providing that the ΔT of 25 K, 30 K, and 80 K are applied, corresponding $V_{oc\text{-}m}$ of 76.962 Mv, 92.354 mV, and 246.278 mV can be calculated. All data is recorded in **Table S5**.

Explanatory note 2

Calculation process of the power generation and maximum power output of the cross-plane TEG

The resistance of a p-type TE leg can be calculated as $r = \frac{l}{\sigma A}$, where l, σ, and A are the length, electrical conductivity, and cross-section of the p-type TE leg, respectively. The total resistance of 8 p-type TE legs is r_p = 8 × 5 mm/(104.3 S cm^{-1} × 2 mm× 23.52 μm) = 81.53 Ω. Likewise, the total resistance of 8 n-type TE legs is r_n is 75.92 Ω. Therefore, the total resistance r_{leg} of the cross-plane TEG is 157.45 Ω. Due to the resistance of liquid metal, the resistance of copper electrodes, and contact resistance between these components, the measured r reaches up to 250 Ω. When the internal resistance r equals the external resistance R, the maximum output power $P_{max\text{-}output}$ occurs.

$V_{oc\text{-}m}$ is the measured open-circuit voltage. $V_{output\text{-}m}$ is the measured voltage of external resistance R. As the cross-plane TEG and the external resistance R are connected in series, the voltage on R can be calculated theoretically to be half of $V_{oc\text{-}m}$ according to the voltage-division principle. $V_{output\text{-}m}$ is 4.936 mV, 10.465 mV, 16.459 mV, 21.770 mV, and 26.669 mV when the ΔT is 3.6 K, 7.1 K, 10.9 K, 14.3 K, and 17.8 K.

Hence, the total power (P_{total}) generated by the cross-plane TEG can be calculated as $P_{total} = (V_{oc\text{-}m})^2/(r+R)$. Based on $P_{max\text{-}output} = (V_{output\text{-}m})^2/R$, $P_{max\text{-}output}$ is 0.098 μW, 0.438 μW, 1.084 μW, 1.896 μW, and 2.845 μW when the ΔT is 3.6 K, 7.1 K, 10.9 K, 14.3 K, and 17.8 K. The $P_{max\text{-}output}$ is 47.94% of P_{total}, slightly lower than the theoretical calculation due to the power consumption of external circuit. Providing that the ΔT of 25 K, 30 K, and 80 K are applied, corresponding $P_{max\text{-}output}$ of 5.792 μW, 8.340 μW, and 59.306 μW can be calculated. All data is recorded in **Table S6**.

Explanatory note 3

Detailed estimation of the detected temperature by each sensing unit of the cross-plane sensor array

The thermovoltage (V_{them}) of a cross-plane temperature sensor under ΔT of 3.6 K, 7.1 K, 10.9 K, 14.3 K, and 17.8 K are measured as 0.847 mV, 1.691 mV, 2.529 mV, 3.720 mV, and 4.455 mV. Hence the V_{them}-ΔT curve is linearly fitted to be $V_{\mathrm{them}} = 0.260\Delta T - 0.138$ ($R^2 = 0.9995$).

When the sensor is attached to a certain surface, the temperature difference in its out-of-plane direction is $\Delta T = T_{\mathrm{m}} - T_0$, where T_0 is the temperature of the reference side, e.g. room temperature, and T_{m} is the temperature of the detected point. So the calculation formula of T_{m} can be derived as $T_{\mathrm{m}} = 3.846V_{\mathrm{them}} + T_0 + 0.533$.

Therefore, for the cross-plane sensor array, the temperature distribution of the detected surface can be concluded based on the measured V_{them} of each sensing unit.

Table S1. Elemental compositions of p-type and n-type Bi_2Te_3 powders.

	Bi (at.%)	Te (at.%)	Sb (at.%)	Se (at.%)
p-type	6.25	68.64	25.11	/
n-type	30.99	66.51	/	2.50

Table S2. FESEM-EDS elemental analysis for p-type 15 vol.%-Bi_2Te_3@PEDOT NW film.

Element	Normalized mass (%)	Atom ratio (%)	Abs. error (%, 1 sigma)
C	24.68	59.99	1.25
O	8.59	15.69	0.42
S	13.89	12.64	0.40
Te	31.30	7.16	0.82
Sb	15.07	3.61	0.41
Bi	6.48	0.90	0.20

Table S3. Component ratios of p-type Bi_2Te_3@PEDOT NW sandwich-like films.

Thickness of total Bi_2Te_3 (μm)	Thickness of PEDOT scaffold (μm)	Volume ratio (vol.%)
2	20	9
3.52	20	15
5.48	20	21.5

Note: n-type 15 vol.%-Bi_2Te_3@PEDOT NW was prepared using the same parameters of thermally depositing.

Table S4. Comparison of TE properties in this work with the data of organic/inorganic composite TE materials reported in the literature at room temperature.

Organic component	Inorganic component	Method	*S*	*PF*	*k*	*zT*	Ref.
PEDOT:PSS	Bi_2Te_3	Electrodeposition	15.2	9.9	0.169	0.0172	1
	Bi_2Te_3 nanosheet	Solution-mixing and drop casting	13.5	32.26	/	/	2
	Bi_2Te_3 particle	Solution-mixing and drop casting	150	131	/	/	3
	Bi_2Te_3 nanowire	Solution-mixing and drop casting	18	10.6	/	/	4
	Bi_2Te_3 nanobarbell	Solution synthesis and drop casting	93.63	60.05	/	/	5
	Bi_2Te_3 nanowire	In situ synthesis and drop casting	24.5	7.45	0.047	0.048	6
	Bi_2Te_3 nanowire	Solution-mixing and spin coating	47	223	/	/	7
	Cu_2Se nanowire	Wet-chemical synthesis and drop casting	50.8	270.3	0.25-0.3	0.3	8
	Te nanorod	Solution-mixing and drop casting	163	70.9	0.22-0.3	0.1	9
	Te nanorod	Solution in-situ synthesis and H_2SO_4-treatment	114.97	284	0.22	0.39	10
	Te nanowire	Solution in-situ synthesis and drop casting	180	35	0.16	0.066	11

	SiC nanowire	Dilution-filtration and post-treatment	20.3	128.3	0.23	0.17	12
	ZnO flower	Spin coating	21	0.4	/	/	13
PEDOT:Tos	Bi_2Te_3 nanoparticles	Lithography and vapor phase polymerization	170	1350	0.7	0.58	14
PEDOT NW	Bi_2Te_3 powder	Solution-mixing and vacuum filtration	10.08	7.49	/	/	15
	Bi_2Te_3 nanowire	Solution-mixing and vacuum filtration	10.8	9.06	/	/	15
P3HT	Bi_2Te_3 nanowire	Solution-mixing and drop casting	86.9	13.6	/	/	16
PANI	SnS nanosheet	In situ synthesis and hot pressing	350	80	0.6	0.04	17
	Ag_2Se nanowire	In situ synthesis and drop casting	97	301.9	/	/	18
	SWNT/Te	In situ synthesis and vacuum filtration	54	101	0.3	0.1	19
PVDF	PANI-coated Ag_2Se nanowire	Solution-mixing and drop casting	85.6	196.6	/	/	18
SWCNT	Bi_2Te_3 nanocrystal	Magnetron sputtering	-147.5	163	0.19	0.25	20
	Bi_2Te_3 nanosheet	Magnetron sputtering	-153	215	0.28	0.23	21
	PPy	In-situ pulse electropolymerization	18	365.2	0.54	0.203	22
	PPy/Te	Sequential pulse	80.9	1602.4	/	/	23

		electrodeposition					
PPy	Te nanocrystal	Electrodeposition	187.5	234.3	/	/	24
	SWCNT	Solution-mixing and vacuum filtration	27	240.3	/	/	25
	Ag_2Se/Se nanostructure	Vacuum filtration and hot pressing	144	2240	/	/	26
PEDOT NW	Bi_2Te_3 nanocrystal	High-vacuum thermal evaporation and thermal-shock	266.4	740.1	0.82	0.27	This work

Note:

The units are μV K^{-1}, μW m^{-1} K^{-2}, and W m^{-1} K^{-1} for S, PF, and κ, respectively.

Abbreviations in **Table S4** and **Fig. 3c** and **d**.

Tos = tosylate; P3HT = poly-(3-hexyl)thiophene; PANI = polyaniline; PVDF = polyvinylidene difluoride; SWCNT = single-walled carbon nanotube; PPy = polypyrrole; P = powder; NB = nanobarbell; NC = nanocrystal; NR = nanorod; NS = nanosheet; NW = nanowire

Table S5. Theoretical and measured open-circuit voltage of the cross-plane TEG.

ΔT (K)	S_p (μV K^{-1})	S_n (μV K^{-1})	N	Equation	$V_{oc\text{-}th}$ (mV)	$V_{oc\text{-}m}$ (mV)
3.6	266.4	-158.1	8		12.226	11.186
7.1	266.4	-158.1	8		24.112	21.772
10.9	266.4	-158.1	8	$V_{oc} = (\lvert S_p\rvert + \lvert S_n\rvert) \times \Delta T \times N$	37.016	33.366
14.3	266.4	-158.1	8		48.563	44.038
17.8	266.4	-158.1	8		60.449	54.706
25	266.4	-158.1	8		84.900	76.962
30	266.4	-158.1	8		101.880	92.354
80	266.4	-158.1	8		271.680	246.278

Note: ΔT is the temperature difference, S_p is the Seebeck coefficient of p-type TE leg, S_n is the Seebeck coefficient of n-type TE leg, N is the number of p-n pairs, $V_{oc\text{-}th}$ is the theoretical open-circuit voltage calculated from the equation, and $V_{oc\text{-}m}$ is the measured open-circuit voltage. The data under the ΔT of 25 K, 30 K, and 80 K is estimated.

Table S6. Total power and the maximum output power of the cross-plane TEG.

ΔT (K)	$V_{\text{oc-m}}$ (mV)	$V_{\text{output-m}}$ (mV)	r (Ω)	Equation	P_{total} (μW)	$P_{\text{max-output}}$ (μW)	$P_{\text{max-output}}/P_{\text{total}}$
3.6	11.186	4.936	250		0.250	0.098	0.392
7.1	21.772	10.465	250		0.948	0.438	0.462
10.9	33.366	16.459	250	$P_{\text{max}} = U^2/4r$	2.227	1.084	0.487
14.3	44.038	21.770	250		3.879	1.896	0.489
17.8	54.706	26.669	250		5.985	2.845	0.475
25	76.962	37.627	250		11.846	5.792	/
30	92.354	45.152	250		17.059	8.340	/
80	246.278	120.405	250		121.306	59.306	/

Note: R is the external resistance, $V_{\text{output-m}}$ is the voltage of external resistance, P_{total} is the total power generated by the cross-plane TEG, and $P_{\text{max-output}}$ is the maximum output power of the cross-plane TEG. The data under the ΔT of 25 K, 30 K, and 80 K is estimated.

Table S7. The detailed data and calculating process of **Fig. 5d**.

Note: Abbreviations in **Fig. 5d**

CNT = carbon nanotube; CNTF = carbon nanotube fiber; CNTY = carbon nanotube yarn

Detailed data in References

Area of TEG (cm^2)	Number of TE legs	Output power (μW)	ΔT (K)	Output power density (μW cm^{-2})	Specific power (nW cm^{-2} K^{-2})	TEG type	Ref
1.5*a1	24	0.224	15	0.149*a2	0.664	Inorganic textile based	68
4*b1	16	0.009	25	2.25×10^{-3}*b2	3.6×10^{-3}	Organic textile based	69
16	20	32*c1	20	2	5	Organic textile based	70
5.59	24	26.553*d1	35	4.75	3.877	Inorganic non-textile based	71
182.25	162	0.32	85.5	4.442×10^{-3}*e1	2.4×10^{-4}	Organic non-textile based	39
4.8	80	2.02	20	0.421*f1	1.052	Organic non-textile based	72
35.5*g1	56	0.2	40	0.0056*g2	3.52×10^{-3}	Organic/inorganic textile based	74
74.4	1932	383.16*h1	47.5	5.15	2.283	Organic textile based	75

4	10	7.16*i1	25	1.79	2.864	Organic textile based	73
6.75	80	6.953*j1	30	1.03	1.144	Organic textile based	76
10.8	72	5.415×10^{-4}*k1	27.7	5.01×10^{-5}	6.534×10^{-5}	Organic textile based	67

Calculation process of the table:

*a1 Calculated data: Fig. 5a presents the dimensions of the TEG with printed 12-couple are 25 mm × 6 mm.

*a2 Calculated data: Fig. 7 presents the output power 0.224 μW at a ΔT of 15 K, so the output power density is about 0.149 μW cm^{-2} from calculating 0.224 μW/(25 mm × 6 mm).

*b1 Calculated data: Fig. 5b presents the dimensions of the TEG are 2 cm × 2 cm.

*b2 Calculated data: Fig. 6a presents the output power 0.009 μW at a ΔT of 25 K, so the output power density is about 2.25×10^{-3} μW cm^{-2} from calculating 0.009 μW/(2 cm × 2 cm).

*c1 Calculated data: Fig. 5a and e present the dimension and the output power density of the TEG.

*d1 Calculated data: Fig. 4a presents dimensions of the TEG are 43 mm × 13 mm. Fig. 5b presents an output power density of 4.75 μW cm^{-2} at a ΔT of 35 K.

*e1 Estimated data: Fig. 2b presents the TEG has dimensions of 18 × 9 elements. From the scale bar the dimensions of one element are about 15 mm × 7.5 mm. So the areal of the TEG is calculated to be 182.25 cm^2. Fig. 3b presents the output power of the TEG is 0.32 μW at a ΔT of 85.5 K.

*f1 Calculated data: Fig. 5a presents the TEG has dimensions of 4 × 5 × 120 mm^3. Fig. 5b presents the output power of the TEG is 2.02 μW at a ΔT of 20 K.

*g1 Estimated data: The length of each TE fiber is about 91 mm and 4 TE fibers with 28 joints are woven into the fabric. So the length of one joint is about 91 × 4 ÷ 28. The dimensions of the TEG in Fig. 4b are about 9.1 cm × 3.9 cm.

*g2 Calculated data: Fig. 4h presents the output power of the TEG with 4 fibers is 200 nW a ΔT of 40 K. So the output power density can be calculated from 200 nW/35.5 cm^2.

*h1 Calculated data: Fig. 4b presents the dimension of the TEG are 9.3 cm × 8 cm. Fig. 4h presents an output power density of 5.15 μW cm^{-2} at a ΔT of 47.5 K.

*i1 Estimated data: Fig. 6a presents the dimension of the TEG are about 2 cm × 2 cm. Fig. 6c presents an output power density of 1.79 μW cm^{-2} at a ΔT of 25 K.

*j1 Calculated data: Fig. 4b presents the dimension of the TEG are about 4.5 cm × 1.5 cm. Fig. 4f presents an output power density of 10.3 mW m^{-2} at a ΔT of 30 K.

*k1 Fig. 5b presents the dimension of the TEG are 3.6 cm × 3 cm. Fig. 5g presents an output power density 501.35 nW m^{-2} at a ΔT of 27.7 K.

Calculation process of the density of TE legs in various cross-section TEGs:

Density of TE legs = Number of TE legs/Area of TEG

Supplementary references

1. Q. Jiang, C. Liu, H. Song, J. Xu and Z. Zhu, *Int. J. Electrochem. Sci.*, 2014, **9**, 7540-7551.
2. Y. Du, K. F. Cai, S. Chen, P. Cizek and T. Lin, *ACS Appl. Mater. Interfaces*, 2014, **6**, 5735−5743.
3. B. Zhang, J. Sun, H. E. Katz, F. Fang and R. L. Opila, *ACS Appl. Mater. Interfaces*, 2010, **2**, 3170-3178.
4. J. Xiong, L. Wang, J. Xu, C. Liu, W. Zhou, H. Shi, Q. Jiang and F. Jiang, *J. Mater. Sci.: Mater. Electron.*, 2016, **27**, 1769-1776.
5. Y. H. K. Eun Jin Bae, Kwang-Suk Jang, Changjin Lee and Song Yun Cho, E. J. Bae, Y. H. Kang, K. S. Jang, C. Lee and S. Y. Cho, *Nanoscale*, 2016, **8**, 10885-10890.
6. W. Thongkham, C. Lertsatitthanakorn, K. Jiramitmongkon, K. Tantisantisom, T. Boonkoom, M. Jitpukdee, K. Sinthiptharakoon, A. Klamchuen, M. Liangruksa and P. Khanchaitit, *ACS Appl. Mater. Interfaces*, 2019, **11**, 6624−6633.
7. W. S. Kim, G. Anoop, I. S. Jeong, H. J. Lee, H. B. Kim, S. H. Kim, G. W. Goo, H. Lee, H. J. Lee, C. Kim, J. H. Lee, B. S. Mun, J. W. Park, E. Lee and J. Y. Jo, *Nano Energy*, 2020, **67**, 10427.
8. Y. Lu, Y. Ding, Y. Qiu, K. Cai, Q. Yao, H. Song, L. Tong, J. He and L. Chen, *ACS Appl. Mater. Interfaces*, 2019, **11**, 12819-12829.
9. K. C. See, J. P. Feser, C. E. Chen, A. Majumdar, J. J. Urban and R. A. Segalman, *Nano Lett.*, 2010, **10**, 4664-4667.
10. E. J. Bae, Y. H. Kang, K. S. Jang and S. Y. Cho, *Scientific reports*, 2016, **6**, 18805.
11. N. E. Coates, S. K. Yee, B. McCulloch, K. C. See, A. Majumdar, R. A. Segalman and J. J. Urban, *Adv. Mater.*, 2013, **25**, 1629-1633.

12. X. Wang, F. Meng, T. Wang, C. Li, H. Tang, Z. Gao, S. Li, F. Jiang and J. Xu, *J. Alloys Compd.*, 2018, **734**, 121-129.

13. Y. Du, K. Cai, S. Z. Shen, W. Yang, J. Xu and T. Lin, *Journal of Materials Science Materials in Electronics*, 2016, **27**, 10289-10293.

14. L. Wang, Z. Zhang, Y. Liu, B. Wang, F. Lei, J. Qiu, K. Zhang and S. Wang, *Nat. Commun.*, 2018.

15. Z. Tian, H. Liu, N. Wang, Y. Liu and X. Zhang, *J. Mater. Sci.: Mater. Electron.*, 2018, **29**, 17367–17373.

16. M. He, J. Ge, Z. Lin, X. Feng, X. Wang, H. Lu, Y. Yang and F. Qiu, *Energy & Environmental Science*, 2012, **5**, 8351-8358.

17. H. Ju, D. Park and J. Kim, *Chem. Eng. J.*, 2018, **356**.

18. D. Park, M. Kim and J. Kim, *J. Alloys Compd.*, 2021, **884**, 161098.

19. L. Wang, Q. Yao, W. Shi, S. Qu and L. Chen, *Materials Chemistry Frontiers*, 2017, **1**, 741-748.

20. Y. Zhao, Y. Li, J. Qiao, S. Jiang and C. Liu, *Carbon*, 2020, **170**, 191-198.

21. Y. Li, J. Qiao, Y. Zhao, Q. Lan and H. Cheng, *Journal of Materials Science and Technology*, 2020, **58**, 80-85.

22. Y. Li, C. Gao, X. Fan and L. Yang, *Chem. Eng. J.*, 2022, **443**, 136536.

23. Y. Li, C. Gao, X. Fan, H. Li and L. Yang, *Advanced Materials Technologies*, 2023, 2201544.

24. Y. Li, C. Gao, X. Fan and L. Yang, *ACS Appl. Mater. Interfaces*, 2022, **14**, 10815-10824.

25. W. Fan, Y. Zhang, C. Y. Guo and G. Chen, *Composites Science and Technology*, 2019, **183**, 107794.107791-107794.107795.

26. Y. Li, Q. Lou, J. Yang, K. Cai, Y. Liu, Y. Lu, Y. Qiu, Y. Lu, Z. Wang, M. Wu, J. He and S. Shen,

Adv. Funct. Mater., 2021, **32**, 2106902.